Simultaneous 3D coincidence imaging of cationic, anionic, and neutral photo-fragments

Abhishek Shahi, Yishai Albeck, and Daniel Strasser (iD)

View Online   Export Citation   CrossMark

ARTICLES YOU MAY BE INTERESTED IN

Simultaneous 3D coincidence imaging of cationic, anionic, and neutral photo-fragments

Abhishek Shahi, Yishai Albeck, and Daniel Strasser[a)]
Institute of Chemistry, The Hebrew University of Jerusalem, 91904 Jerusalem, Israel

We present the design and simulations of a 3D coincidence imaging spectrometer for fast beam photofragmentation experiments. Coincidence detection of cationic, neutral, and anionic fragments involves spectrometer aberrations that are successfully corrected by an analytical model combined with exact numerical simulations. The spectrometer performance is experimentally demonstrated by characterization of four different channels of intense 800 nm pulse interaction with F_2^-: $F^- + F$ photodissociation, $F + F$ dissociative photodetachment, $F^+ + F$ dissociative ionization, and $F^+ + F^+$ coulomb explosion. Improved measurement of F_2^- photodissociation with a 400 nm photon allows a better determination of the F_2^- anion dissociation energy, 1.256 ± 0.005 eV. *Published by AIP Publishing.* https://doi.org/10.1063/1.5004523

I. INTRODUCTION

Fragment imaging techniques provide detailed information about photodetachment, photoionization as well as other dissociation processes.[1–4] In such experiments, angular resolved kinetic energy release (KER) is obtained by imaging the 2D position and sometimes also the time of a fragment arrival to a position sensitive detector, allowing 3D velocity reconstruction. One of the broadly implemented fragment imaging methods is velocity map imaging (VMI), introduced by Eppink and Parker.[5,6] VMI takes advantage of a specially designed electrostatic lens that accelerates charged fragments to a position sensitive detector while achieving mapping of the 2D fragment velocities onto positions on the detector surface, independent of their initial position. VMI imaging is successfully implemented to study different charged fragments including angularly resolved photoelectron spectroscopy and imaging of cationic products of dissociative ionization or of anions produced by dissociative electron attachment.[6–8] Coincidence detection of correlated charged fragments from a single parent molecule, such as photoelectron photoion coincidence spectroscopy (PEPICO), allows us to disentangle competing fragmentation mechanisms based on fragment correlations.[9,10] Using a clever combination of electrostatic and magnetic fields to map photoions and photoelectrons on two separate imaging detectors, the so-called COLTRIMS experiments (cold target recoil ion momentum spectroscopy) provide complete information about the charged products of dissociative ionization events.[11–13]

In both VMI and COLTRIMS experiments, only charged fragments can be detected as acceleration to ~1 keV is necessary to achieve efficient single ion detection.[14] Information about neutral products of dissociation can in some cases be obtained by selective ionization of neutral species of interest.[15–17] By contrast, techniques using fast ion beam targets allow direct detection of neutral fragments, produced in the moving molecular frame of reference, due to initial velocity in the laboratory frame.[18–22] Continetti and co-workers integrated VMI photoelectron imaging with a fast anion beam setup for neutral fragment imaging, allowing it to disentangle KER spectra originating from different neutral electronic states initiated by photodetachment from an anion precursor.[23,24] Ben-Itzhak and co-workers developed a photofragment spectrometer combined with a fast cation beam for coincidence detection, resolving cationic and neutral dissociation products.[25–27]

Using a fast anion beam target and a similar concept of an electrostatic spectrometer, we are able to investigate different competing dissociation and electron detachment channels in intense field interaction with atomic, molecular, and cluster anions.[28–33] The photofragment spectrometer design allows coincidence detection of all the possible dissociation products on the same detector, including the anionic, cationic, and neutral fragments. In the present study, we describe the design, calibration, and optimization of the photofragment spectrometer as well as an analytic model for extracting channel specific KER spectra from 3D coincidence imaging data. Detailed simulations that allow us to calibrate and improve the spectrometer resolution are presented and compared to experimental F_2^- photodissociation measurements, providing an improved value for the F_2^- dissociation energy. In the following, we describe the experimental setup, the analytic model for the spectrometer response, and the detailed ion trajectory simulations and compare our previously published experimental F_2^- dissociation measurements[33] to the new data collected with the improved spectrometer design.

II. EXPERIMENTAL SETUP

In our experimental setup,[28–32] anions are produced in a cold ion source, equipped with a pulsed electron gun and an Even-Lavie pulsed valve.[34] F_2^- anions are formed

---

a)strasser@huji.ac.il

by dissociative electron attachment to the NF_3 precursor sample,[35,36] supersonically expanded with Ar carrier gas. The anions are accelerated to an E_0 kinetic energy in a pulsed Wiley-McLaren time-of-flight (TOF) mass spectrometer[37] and directed towards the photofragment spectrometer. Figure 1 shows the experimental scheme of the spectrometer. At the entrance to the spectrometer, a pulsed deflector is used as a mass gate for mass selection of target anions based on their TOF. The spectrometer electrodes are 1 mm thick plates with 60 mm outer diameter. The first grounded electrode together with the interaction region electrode acts as a collimator, with a 5 mm inner diameter defining the ion beam width. The next electrodes are spaced by 5 mm and permit a uniform increase of the spectrometer potential from ground to U_{sp}. This allows the acceleration of the parent anions before they reach the ion-laser interaction region. In the 10 mm long field free inter-action region, the ion bunch is crossed by a focused laser beam. The ion bunch arrival time to the interaction region is synchronized to the time of the femtosecond laser pulse by triggering the experiment on the previous cavity dump sig-nal. The laser timing provides 1 amu resolution and allows us to target F_2^- rather than $F^- \cdot (H_2O)$ clusters which were both present in the ion beam. At the exit side of the spectrome-ter, the electrode potentials are uniformly decreased over a distance D from U_{sp} to zero, except one asymmetric elec-trode labeled U_{as}. Thus, while anions are decelerated, neutral products maintain their velocity and cations are accelerated by the spectrometer potential. The asymmetric U_{as} potential is introduced to prevent the acceleration of residual gas ion-ization products towards the detector. The focusing effect of this lens on the charged fragment trajectories is discussed in detail in Secs. III and VI. The fragments travel in a field-free region to the MCP detector placed at a distance L from the cen-ter of the ion-laser interaction region. The E_0, U_{sp}, and U_{as} potentials are chosen such that all fragments of interest reach the detector with sufficient energy for efficient single particle detection.[14] The electronic timing signals are digitized by a fast scope and 2D position information is captured by imaging the phosphor anode surface using a high-frame-rate CCD cam-era.[38,39] The data are transferred to a computer that implements a fast 1D peak finding routine to extract the TOF's and pulse amplitudes from the electronic signal and a fast 2D peak find-ing routine to extract positions and brightness of the coincident optical signals. We use the correlation of the amplitude of the electronic timing signal and the brightness of the optical position signal of a specific hit to correlate the times and posi-tions of multiple hits.[32,40–42] In Sec. III, we explain how the position and timing information are analyzed to extract the 3D KER.

III. MODEL DESCRIPTION

While exact numerical treatment is possible with present computational capabilities, analytic modeling allows speeding up of large data set analysis in real time. We begin mod-eling of the ion trajectories from the ion-laser interaction region where a parent anion of mass M with an initial kinetic energy E_0 has been accelerated by the spectrometer potential, U_{sp}, to a total kinetic energy of $E_0 + U_{sp}$. Photofragments of mass m are accelerated or decelerated according to their charge q as they exit the spectrometer, reaching to a final velocity, v_0,

$$v_0 = \sqrt{2\left(\frac{E_0 + U_{sp}}{M} + \frac{q}{m}U_{sp}\right)}. \tag{1}$$

The dependence of v_0 on the fragments' charge over mass ratio, q/m, allows distinguishing different products based on their TOF, t_0, to the detector located at distance L as

$$t_0 \approx \frac{\tilde{L}}{v_0}, \tag{2}$$

where $\tilde{L}$ is an effective distance, reflecting the different velocity of charged fragments within the short acceleration or decel-eration region in the spectrometer potential. In the following, we describe the analytic model for the KER construction from fragment recoil along the TOF axis of the spectrometer and the radial direction.

A. Recoil along the TOF axis

In the case of dissociation, the recoil of a fragment along the TOF axis (Z-direction) results in a different TOF, t, that
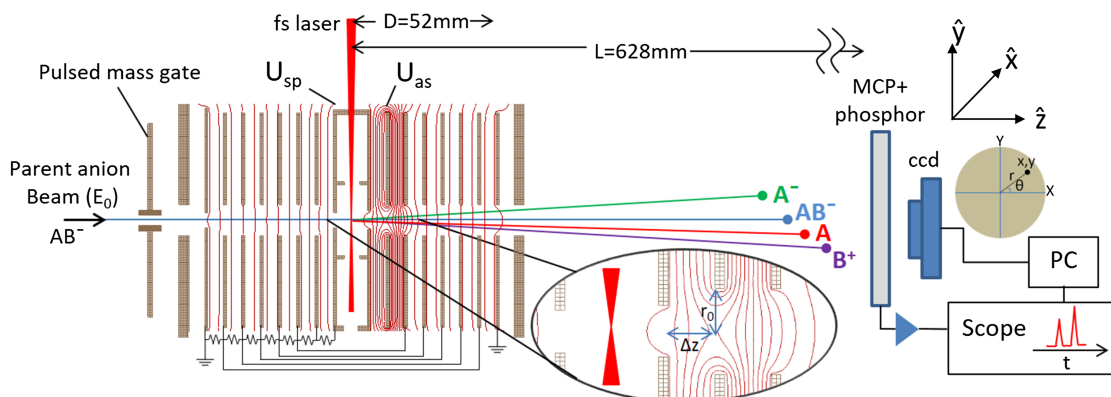

FIG. 1. Scheme for the experimental setup. Potential contours presented by solid red lines are equally separated by 50 V from 10 V to 960 V. The TOF and position information are recorded by a scope and CCD, respectively.

can be related to the recoil velocity Δv_z,

$$\Delta v_z = \frac{\tilde{L}}{t} - \frac{\tilde{L}}{t_0}. \tag{3}$$

We can therefore derive the recoil kinetic energy of the fragment along the TOF axis as $\frac{1}{2}m\Delta v_z^2$, and for relatively small recoil times $(t - t_0) \ll t_0$, it can be approximated as

$$KER_z = \frac{1}{2}m\left(\frac{\tilde{L}_q}{t_0}\right)^2\left[\left(\frac{t - t_0}{t_0}\right)^2 - 2\left(\frac{t - t_0}{t_0}\right)^3\right]. \tag{4}$$

It is valuable to emphasize the cubic term in Eq. (4) that accounts for the asymmetry between recoil in the direction of parent ion motion towards the detector and recoil away from the detector. For neutral fragments, the optimal effective distance $\tilde{L}_{q=0}$ is strictly equal to the actual distance to the detector L. However, for charged fragments, the propagation in the acceleration or deceleration region results in a small correction of the effective distance. An approximate qualitative expression for the correction factor can be obtained by considering a uniform acceleration/deceleration field that is equal to the potential drop over the distance D from the U_{sp} potential at the ion-laser interaction region to ground at the exit of the spectrometer. The total TOF (with no recoil) can be then expressed as

$$t_0 = \frac{L(1 + a_q)}{v_0}, \tag{5}$$

where under the approximation that the final kinetic energy is significantly higher than the spectrometer potential, we can obtain that the acceleration correction factor, a_q, for the effective length $\tilde{L}_q = L\left(1 + a_q\right)$ is given by

$$a_q \approx \frac{D}{2L}\frac{qU_{sp}}{mV_0^2}. \tag{6}$$

For cationic fragments, a_q is positive due to slower speed during the acceleration in the spectrometer field, corresponding to a longer effective distance traveled at the final velocity v_0. Anionic fragments that are decelerated in the spectrometer will have a negative a_q correction. The overall magnitude of the correction factor depends on the geometric $D/2L$ ratio and decreases with U_{sp}/E_0. The exact quantitative a_q value depends on the detailed geometry of the spectrometer potential and will therefore be obtained in Sec. IV A by fitting simulated ion trajectories. The analytic expression of Eq. (4) for KER_z can be used to calculate also the fragment momentum along the Z-axis in the frame of the parent anion according to

$$\Delta P_z = sgn(t_0 - t)\sqrt{2mKER_z}, \tag{7}$$

where the momentum recoil direction is determined based on the sign of the TOF, t, deviation from the expected zero recoil, t_0.

B. Radial recoil

KER in the XY plane of the detector will result in a radial recoil that reaches a distance r during the TOF to the detector. The cylindrical symmetry of the spectrometer setup makes it natural to convert the measured (x, y) to $r = \sqrt{x^2 + y^2}$ and

$cos\,\theta = \frac{x}{r}$. Thus, the radial KER component can be calculated from the measured position recoil, r, and TOF, t, according to

$$KER_r = \frac{1}{2}m\left(\frac{r}{t}\left(1 + \mathcal{F}_q\right)\right)^2. \tag{8}$$

Similar to the acceleration correction factor introduced in Eq. (5), we introduce a dimensionless focusing factor $\mathcal{F}_q$ to correct for the focusing of charged fragment trajectories by the spectrometer potential. As shown by the equal-potential contours in Fig. 1 (inset), an electrostatic lens is created by the asymmetric electrode U_{as} potential. As the kinetic energy of the parent ion is significantly higher than the lens potential, the effect of the lens can be effectively corrected by the focusing factor $\mathcal{F}_q$ introduced into Eq. (8). A qualitative expression for $\mathcal{F}_q$ can be derived by calculating the radial velocity change as the fragment ion propagates across the electrostatic field, $E_r(r, z)$, along the lens region,[43]

$$\delta v_r = \frac{q}{m}\int \frac{E_r(r, z)}{v_z}dz. \tag{9}$$

For the purpose of deriving an approximate qualitative expression for $\mathcal{F}_q$, we consider that within the lens region, the radial potential can be approximated by a harmonic potential, resulting in a radial field of the form

$$E_r(r, z) \approx \frac{2\Delta U_{as}^* r}{r_0^2}, \tag{10}$$

where r_0 represents the inner radius of the U_{as} electrode and ΔU_{as}^* is the potential difference between the U_{as} potential applied to the electrode and the potential on the spectrometer axis. We consider that the lens extends effectively along an $\sim\!\Delta z$ spacing between the electrodes and that the radial displacement in the lens region is mainly due to the radial recoil of $\Delta v_r \times \Delta z$, we thus obtain

$$\mathcal{F}_q \approx -2\left(\frac{\Delta z}{r_0}\right)^2\frac{M}{m}\frac{q\Delta U_{as}^*}{(E_0 + U_{sp})}\left(1 - \frac{M}{m}\frac{q\Delta U_{as}^*}{(E_0 + U_{sp})}\right). \tag{11}$$

Under our weak focusing conditions, the term $(M/m)\Delta U_{as}^*/(E_0 + U_{sp}) < 1$. Thus, for anions, the sign of $\mathcal{F}_q$ will always be positive, reflecting focusing of the fragment trajectories. By contrast, cation trajectories are defocused, resulting in negative $\mathcal{F}_q$. We also note that as ΔU_{as}^* is positive, a larger magnitude of the focusing correction is expected for anions in comparison to cations. Although the applied lens potential is electrostatic, which is typically mass independent,[43] the ion trajectories exhibit mass dependent focusing that arises from the fragment energy dependence on mass.

Similar to the acceleration correction factor, the quantitative value of the ion focusing correction depends on the exact geometry of the spectrometer potential and will be obtained by fitting simulated ion trajectories. The obtained analytic expression for the radial KER_r allows calculating the projection of the radial momentum in the XY plane according to

$$\begin{aligned}\Delta P_x = \cos(\theta)\sqrt{2mKER_r}\\ \Delta P_y = \sin(\theta)\sqrt{2mKER_r},\end{aligned} \tag{12}$$

where θ is the recoil angle relative to the X-axis, as shown in Fig. 1.

IV. NUMERICAL SIMULATION

The SIMION[44] simulation includes the photofragment spectrometer and detector region at the exact experimental geometry described in Sec. II and Fig. 1. For the simulation of the F_2^- photodissociation experiments,[33] the initial parent anion energy is set to $E_0 = 2.3$ keV, where the U_{sp} and U_{as} potentials supplied to the spectrometer electrodes are set to +0.6 keV and +0.95 keV, respectively. Under these conditions, the electrostatic lens potential shown in Fig. 1 (inset) results in weak focusing of the parent anion beam with a low effective focal length $\geq 2L$. Upon reaching the laser interaction region at the center of the spectrometer, the parent anion mass and charge are changed to those of the simulated photofragment species and an additional velocity is added according to the simulated kinetic energy release. In Subsections IV A–IV D, we describe the simulation of (A) recoil along the TOF axis, (B) radial recoil in the plane of the MCP detector, (C) coincidence 3D analysis of isotropic dissociation, and (D) analysis of realistic dissociation data.

A. Recoil along the TOF axis

Figure 2 shows the simulated t_0 times, corresponding to a zero KER, as a function of product charge over mass ratio. The full line indicates that the simulated times fit the approximated functional form of Eq. (2), using an effective length fit parameter $\tilde{L}$.

Figure 3 shows the simulated TOF for the possible fragment species: the F^+ cation, the neutral F, and the F^- anion. For each species, TOF's are simulated for different KER_z, corresponding to recoil along the TOF axis towards or away from the detector. The full lines represent a fit of the simulated KER_z as a function of the TOF recoil using Eq. (4). The neutral fragments do not experience an additional acceleration or deceleration. Accordingly, the fitted L and E_0 parameters are found to strictly match the simulated distance to the detector and the initial beam energy. For the charged fragment fits, the only free fit parameter is a_q that is determined to be −0.22 for F^- and +0.17 for F^+. The estimation of a_q from the qualitative expression of Eq. (6) gives −0.03 and +0.01 for the anion and cation, respectively. As mentioned, the exact values depend on the specific geometry of the spectrometer potentials and are
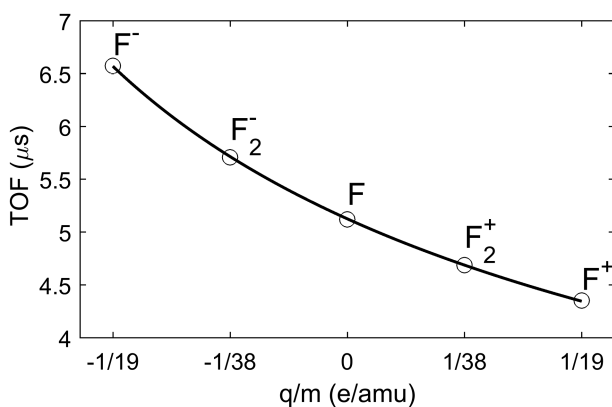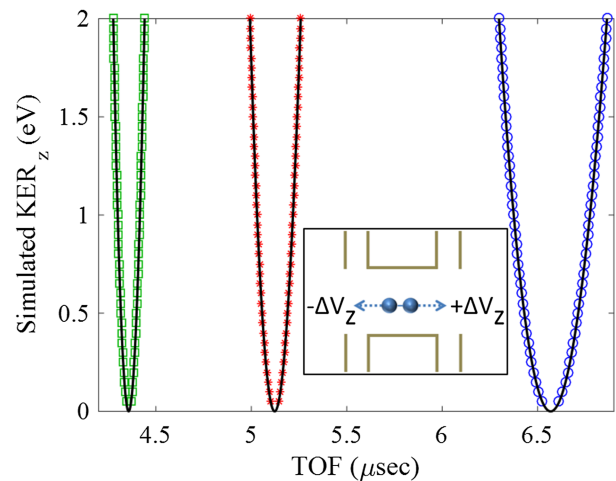

FIG. 3. Simulated KER_z as a function of the TOF recoil. (blue circles) for F^- anion, (red asterisks) for F neutral, and (green squares) for F^+ cation. The inset shows the simulated recoil velocity of two fragments in the Z-direction, $\pm\Delta V_z$, in the parent anion center-of-mass frame.

not expected to be directly obtained from the approximated Eq. (6). Nevertheless, the fitted sign of the acceleration correction factor, corresponding to a shorter effective length $\tilde{L}_{(-)}$ for the anion and a longer $\tilde{L}_{(+)}$ for the cation product, as well as the larger correction magnitude for the decelerated species is in qualitative agreement with the approximated expression of Eq. (6).

As in our realistic experimental conditions, the parent anion beam is produced in a Wiley-McLaren type acceleration scheme;[37] it can exhibit up to an ~200 eV spread of the initial parent anion kinetic energy E_0. We, therefore, simulate the chromatic aberrations of the ion TOF as a function of the simulated beam energy E_0. Figures 4(a) and 4(b) show the chromatic aberrations to the fitted parameters as a function of the initial parent ion energy, E_0. The 200 eV energy spread leads to maximum ±2% chromatic aberration of the calculated KER_z. As expected from Eq. (6), the $|a_q|$ magnitudes are decreasing with increasing beam energy E_0. As the considered 200 eV spread is small with respect to the parent anion kinetic energy at the center of the spectrometer, the chromatic aberrations effect can be treated as a first order perturbation as demonstrated in Figs. 4(a) and 4(b).

B. Radial recoil in the plane of the MCP detector

Figure 5 shows the correlation between the simulated KER_r in the radial direction and the radial recoil on the detector over the TOF for the F^+, F, and F^- fragments. For neutral fragments that are not affected by the electrostatic lens, the r/t ratio is strictly equal to the radial recoil velocity, resulting in a quadratic relation expressed in Eq. (8), where $\mathcal{F}_{q=0} = 0$. For charged fragments, the ion lens results in focusing of the negatively charged fragments and slight defocusing of the positively charged photofragment trajectories. As shown in Fig. 5 by the solid lines for all three fragment species, the simulated KER_r as a function of calculated r/t is successfully described by Eq. (8), where $\mathcal{F}_q$'s are used as free fitting parameters: $\mathcal{F}_{(-)} = +0.18$ for anion, where the positive sign accounts for the focusing anions trajectories, and $\mathcal{F}_{(+)} = -0.04$, fitted for the
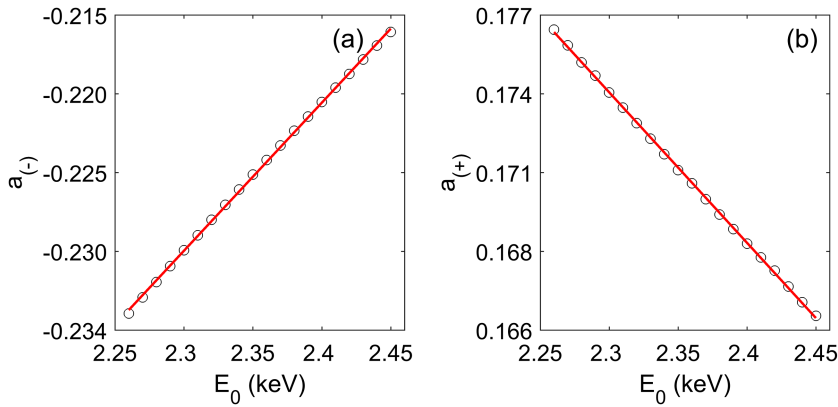

FIG. 2. Simulated TOF, t_0, (°) as a function of q/m for zero KER. Solid line represents a fit of the simulated TOF's with Eq. (2).

FIG. 4. $\circ$ shows the simulated acceleration factor as a function of the initial parent ion energy (E_0), where panel (a) shows the $a_{(-)}$ focusing of the anionic fragments and panel (b) shows the $a_{(+)}$ focusing factor for the cationic products of F_2^- dissociation. Solid red lines show the fitted first order linear approximation.

defocused cation product trajectories. The qualitative expression for the focusing correction derived from Eq. (11) overestimates the focusing. Nevertheless, the sign and the relative magnitude of the anion (0.31) and cation (−0.23) corrections are in qualitative agreement with the fitted $\mathcal{F}_q$ factors. Similar to the chromatic aberrations in a_q, discussed in Sec. IV A, the focusing dependence on the energy E_0 contributes to less than ±2% in the relevant range of parent ion energy spread. Figures 6(a) and 6(b) show a rough linear fit for $\mathcal{F}_q$ dependence on the parent ion beam energy for anion and cation, respectively. As expected from the qualitative description given in Eq. (11), the magnitude of both positive and negative focusing correction factors is reduced with increasing parent ion beam energy.

C. Coincidence 3D analysis of isotropic dissociation

In this section, simulated KER of isotropic dissociation channels is compared to calculated KER based on the fitted analytical expressions relating simulated r and t to KER_r and KER_z. Experimentally, four competing processes have been observed for the dissociation of the F_2^- anion by intense fs laser pulses, which are photodissociation (F$^-$ + F), dissociative photodetachment (F + F), dissociative ionization (F$^+$ + F),
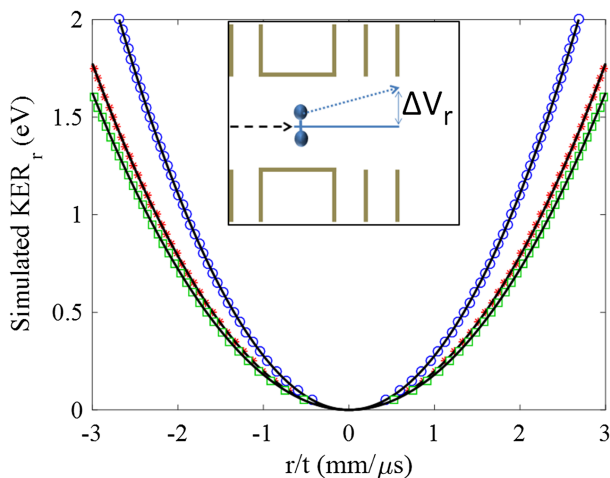

FIG. 5. Simulated r/t as a function of KER. (blue circles) for F^- anion, (red asterisks) for F neutral, and (green squares) for F^+ cation. The fits to Eq. (8) are shown by solid lines. The inset shows the simulated radial recoil velocity, ΔV_r, in the parent anion center-of-mass frame.

and Coulomb explosion (F$^+$ + F$^+$).[33] Coincidence detection of all the fragments that are ejected from a single molecule at a time allows taking advantage of total momentum conservation to correct chromatic aberrations in an iterative procedure. First, the sum of all the coincidence fragment momenta of a specific fragmentation event $\Delta P_z^{cm} = \sum \Delta P_z$ is estimated using Eq. (4), Eq. (7), and an average E_0 value. The calculated center-of-mass momentum in the moving frame can then be used to evaluate a kinetic energy correction for each specific parent anion according to

$$\Delta E_0 = \Delta P_z^{cm} \sqrt{\frac{2(E_0 + U_{sp})}{M}}. \tag{13}$$

KER_z and KER_r can then be calculated for each fragment, using the corrected parameters according to the linear fits shown in Figs. 4 and 6. The radial component of the center-of-mass momentum can also be calculated and corrected by calculating the total KER in the center-of-mass frame of reference determined by

$$\begin{aligned} \Delta P_x^{cm} &= \sum \Delta P_x, \\ \Delta P_y^{cm} &= \sum \Delta P_y. \end{aligned} \tag{14}$$

For each channel, a total of 2×10^5 particles are simulated, limiting the statistical error to ±0.1%. Figure 7 compares the calculated total KER to the simulated KER for four different fragmentation channels assuming isotropic dissociation, a uniform 200 eV spread of the parent anion energy E_0, and a realistic parent anion beam divergence within an ~1° cone. The vanishing deviations from the diagonal line indicated in Figs. 7(a)–7(d) indicate a successful reconstruction of the simulated 3D KER with a standard deviation of ≲0.1% for KER at ~2 eV. While the reconstruction of two neutral fragments' KER is exact within the numerical error of the simulation, the approximated expressions for charged fragments introduce a small error to the calculated KER. As shown in Fig. 7 (insets), the δKER error which is slightly more significant for the F$^-$ + F channel reaches a standard deviation of less than 1% at 2 eV KER.

D. Coincidence 3D analysis of realistic dissociation data

In addition to the intrinsic spectrometer resolution, we simulate also our typical instrumental errors that include an ~1 ns time resolution of our scope and fast 1D peak finding
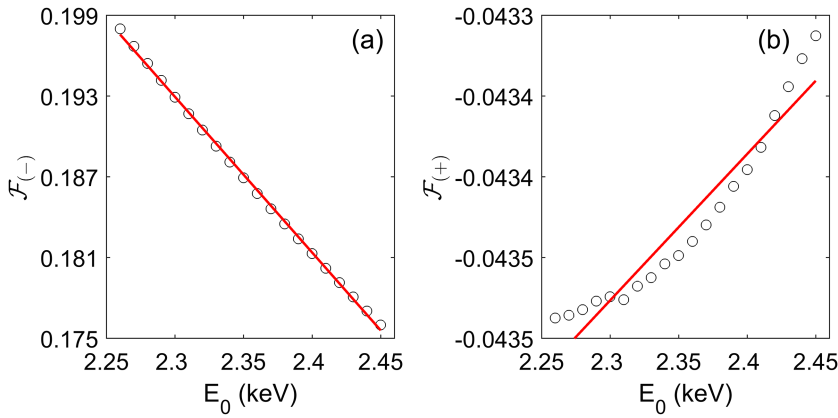
FIG. 6. ° shows the simulated focusing factor $\mathcal{F}_q$ as a function of the initial parent ion energy, E_0. Panel (a) shows the $\mathcal{F}_{(-)}$ focusing of the anionic fragments and panel (b) shows the $\mathcal{F}_{(+)}$ focusing factor for the cationic products of F_2^- dissociation. Solid red lines show the fitted first order linear approximation, used to correct the chromatic aberrations of the calculated KER within better than 0.1%.

routine, an $\lesssim$10 ns laser trigger jitter, and ~100 μm position resolution of the CCD digitization of the phosphor anode and our fast 2D peak finding routine. Furthermore, as can be seen from Fig. 1, the laser-ion interaction region is well confined in the X and Z dimensions within the ~25 μm waist of the focused laser beam. By contrast, the laser-ion interaction region is extended in the $\hat{Y}$ direction of laser propagation across the width of the parent ion beam that had a $\leq$5 mm diameter in our original spectrometer design. This is particularly important for linear processes, such as photodissociation of F_2^- with 400 nm photons that is not confined to the intense focused region of the laser. Figure 8 compares the calculated total KER to the simulated KER for the four different fragmentation channels, assuming isotropic dissociation and taking into account all the realistic experimental errors mentioned above, including the parent anion beam energy spread and beam divergence

that were introduced in Sec. IV C. Surprisingly, while the reconstructed KER error of the symmetric channels F + F and F^+ + F^+ are well below ~2%, the asymmetric channels F^- + F and F^+ + F exhibit ~10% δKER spread.

Similar to spatial aberrations in regular optics,[43] ion imaging is sensitive to the initial off-axis position. Such initial position shift of the parent anion is not correctly subtracted by the center-of-mass momentum correction according to Eq. (14) and results in a residual KER error. Neglecting the focusing and acceleration corrections, we obtain the following approximate expression for the resulting δKER error:

$$\delta KER \approx \Delta P_y Y_0 \left(\frac{1}{t_1} - \frac{1}{t_2} \right), \qquad (15)$$

where ΔP_y is the recoil momentum component in the $\hat{Y}$ direction, Y_0 is the initial position offset, and t_1 and t_2 are the
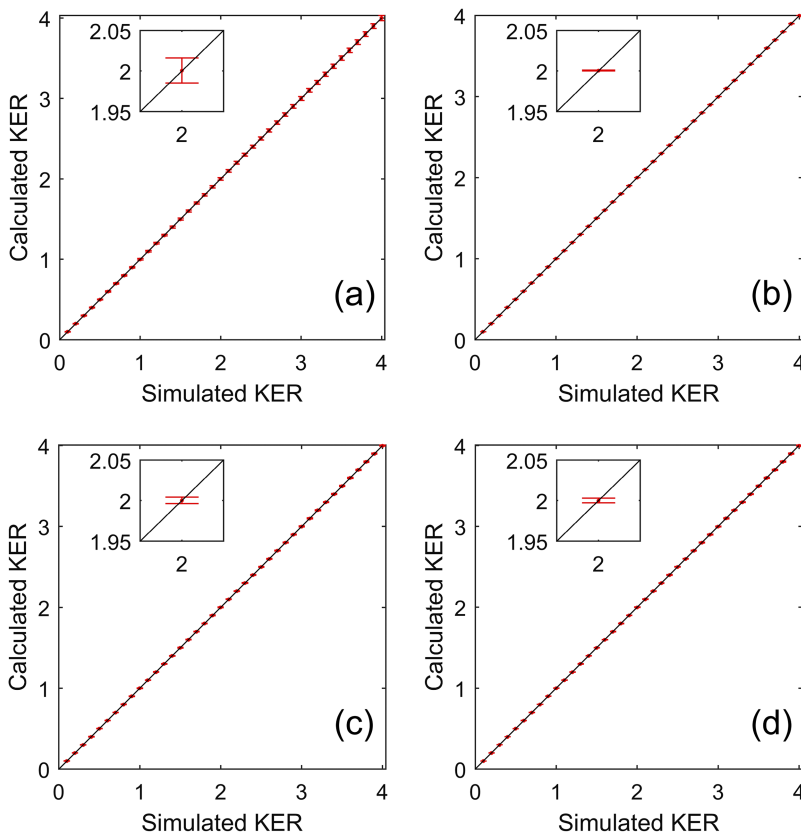

FIG. 7. Calculated KER and KER errors as a function of simulated KER, with 200 eV beam energy spread and 1° ion beam divergence for (a) F^- + F, (b) F + F, (c) F^+ + F, and (d) F^+ + F^+ channels. Error bars indicate the standard deviation of the calculated KER from the simulated value. Insets show zoomed-in views at 2 eV KER with identical scaling of the axes for all four channels.
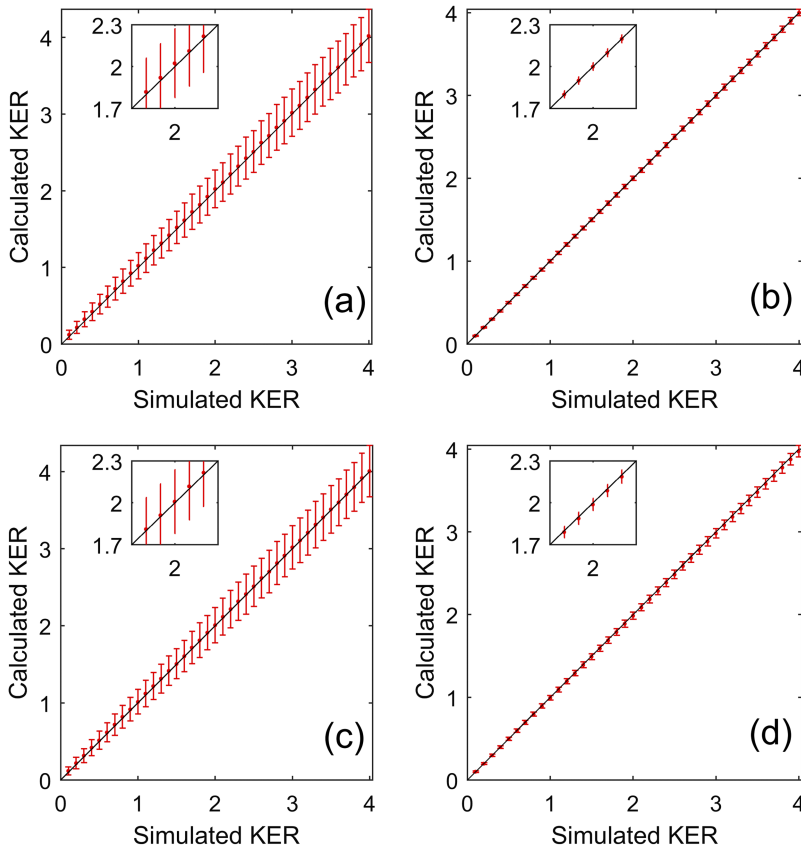
FIG. 8. Calculated KER and KER errors as a function of simulated KER for (a) $F^- + F$, (b) $F + F$, (c) $F^+ + F$, and (d) $F^+ + F^+$ channels. The included uncertainties in the simulations are 5 mm ion beam width, 200 eV beam energy spread, 1° ion beam divergence, and instrumental errors as described in the text. Error bars indicate the standard deviation of the calculated KER from the simulated value. Insets show zoomed-in view at 2 eV KER and its axes are identically scaled.

TOF's of the two fragments. As ΔP_y can either point in the same or opposite direction as Y_0, the result is a symmetric broadening around the correct KER values. Considering, for example, the maximal ~2.5 mm off-axis displacement in our original experimental setup and the typical TOF's of F and F^- shown in Fig. 2, an ~2 eV KER can be expected to contribute few percent to the KER peak broadening. Interestingly, in the case of symmetric $F + F$ or $F^+ + F^+$ channel, for which $1/t_1 \approx 1/t_2$, Eq. (15) predicts negligible δKER in agreement with Fig. 8 simulation. Figure 9 shows the simulated KER error at ~2 eV as a function of ion beam diameter. As can be expected from Eq. (15), the standard deviation of the calculated KER shows a significant increase for the asymmetric channels, while symmetric channels are less sensitive to the initial position spread. We conclude that an ~2 mm parent ion beam width will allow the optimal balance between signal rate, which is proportional to the beam width, and KER resolution. Based on these guidelines, we modified our experimental setup as presented in Sec. V.

V. EXPERIMENTAL RESULTS

We performed the photodissociation experiment of F_2^- anion interacting with 800 nm intense laser pulse using the experimental setup mentioned in Sec. II. We successfully observed four competing channels and their KER.[33] In Fig. 10(a), the observed KER peak for channel $F^- + F$ is centered at ~0.4 eV which is assigned to a combination of linear and nonlinear processes.[33] Figure 10(b) shows low KER for the $F + F$ channel similar to the $F^- + F$ channel, which is

assigned to a dissociation of F_2^- anion followed by detachment of an electron from atomic F^-.[33] Figure 10(c) shows two competing processes identified by low and high KERs for the $F^+ + F$ channel. The low KER, similar to the $F + F$ channel, represents a sequential process of dissociation followed
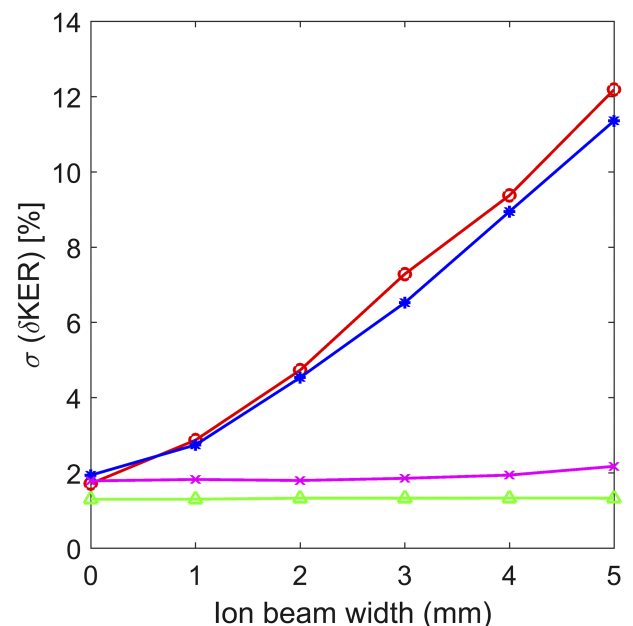

FIG. 9. Standard deviation of the calculated δKER error as a function of ion beam width, for simulated 2 eV KER events of: (red circles) $F^- + F$, (blue asterisks) $F^+ + F$, (green triangles) $F + F$, and (magenta crosses) $F^+ + F^+$ channels.
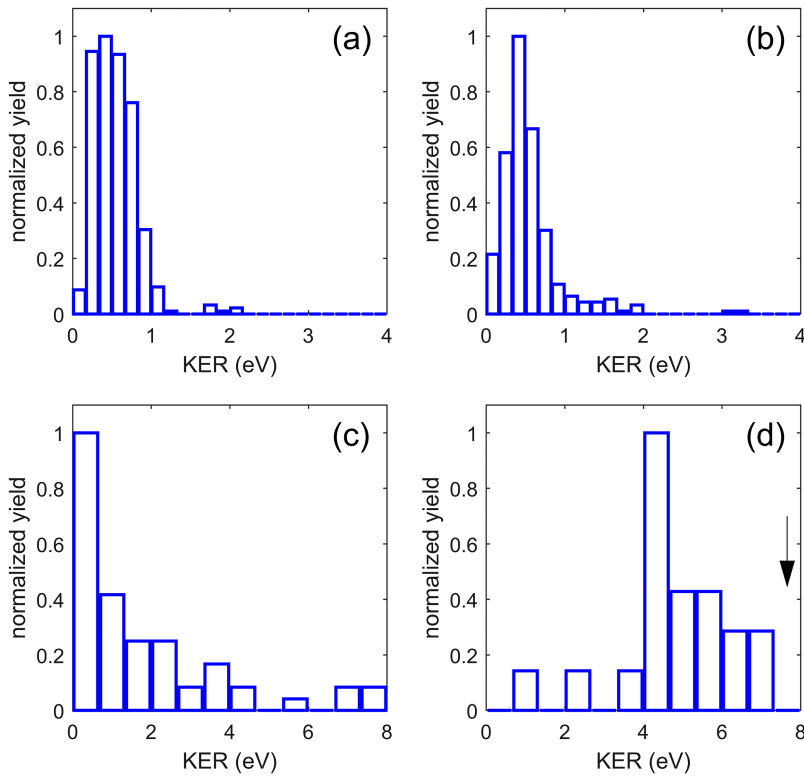
FIG. 10. Experimentally measured KER spectra with intense 800 nm pulses for (a) $F^- + F$, (b) $F + F$, (c) $F^+ + F$, and (d) $F^+ + F^+$ channels. Arrow indicates the theoretical KER from a pure coulomb explosion from the 1.88 Å F_2^- anion bond length.

by instantaneous removal of two electrons from F^-, whereas the high KER is assigned to a non-sequential process, i.e., removal of two electrons from F_2^- anion followed by dissociation.[33] The $F^+ + F^+$ channel is a Coulomb explosion, presented in Fig. 10(d), and is characterized with high KER, expected from an instantaneous removal of 3 electrons by the intense

laser pulse, resulting in a strong Coulombic repulsion at short distances.[33]

In contrast to the intense 800 nm data showing competing nonlinear mechanisms, the $F^- + F$ photodissociation by low 400 nm field is expected to be governed by a linear mechanism. The KER distribution from interacting with low
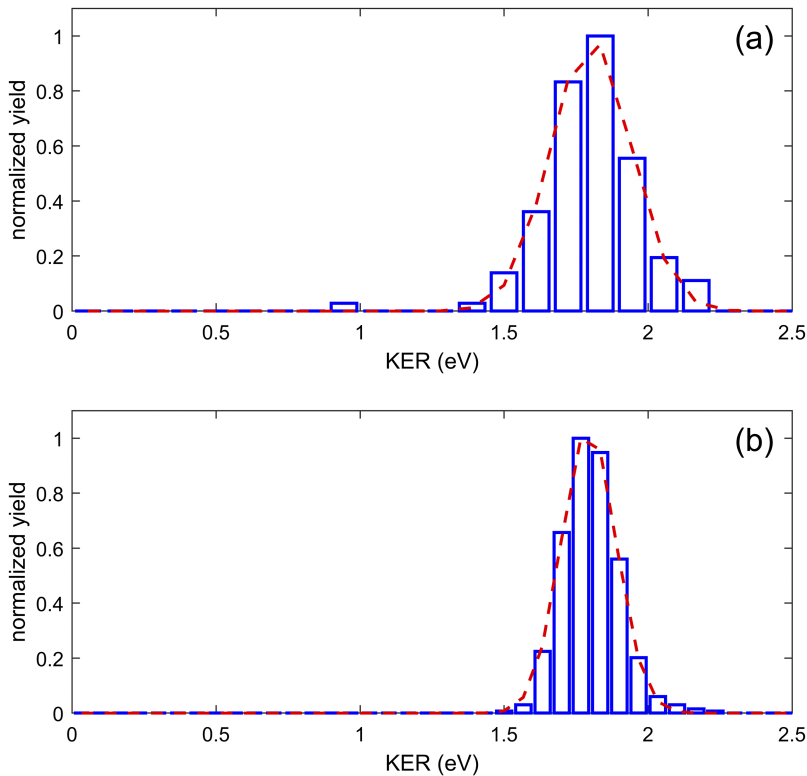

FIG. 11. Experimentally measured KER spectra of the $F^- + F$ photodissociation channel with 400 nm pulses. The improved KER resolution measured for reduced ion beam width is demonstrated by comparing spectra recorded with (a) 5 mm and (b) 2 mm ion-beam widths.

field 400 nm femtosecond laser is shown in Fig. 11 for the $F^- + F$ channel. Figure 11(a) shows an improved analysis of the previously reported data collected with the ~5 mm beam width. The measured KER peak is centered at 1.79 ± 0.01 eV and the width of the peak is fitted with $\delta KER = 0.14$ eV. According to Fig. 9, the ~8% error suggests an actual beam width smaller than the 5 mm diameter of the spectrometer electrodes.

Nevertheless, based on the findings from simulation in Sec. IV D, we decided to further limit the beam diameter by reducing the inner diameter of the collimating electrodes from 5 mm to 2 mm. The aperture size of the electrode after the ion-laser interaction region was also changed from 6 mm to 3 mm. We repeated the F_2^- photodissociation experiment with low field 400 nm wavelength using our improved setup. Figure 11(b) shows the new data, reflecting the improve δKER. As predicted by Eq. (15), the peak position remains at 1.794 (± 0.005) eV where the dominant error source is due to the systematic calibration error of our exact spectrometer dimension. The improved δKER width of ~0.095 eV is in agreement with the expected experimental error convoluted with the ~0.056 eV broadening due to the laser bandwidth and ~100 K rotational temperature of the parent anion. The improved δKER translates also into a smaller error for the KER peak, thus allowing a lower error for the F_2^- dissociation energy, which is obtained from the $h\nu = 3.1$ eV photon energy minus the measured 1.794 ± 0.005 eV KER and the 50 meV internal spin-orbit excitation of the F atom product.[45] This amounts to an F_2^- dissociation energy of 1.256 ± 0.005 eV.

VI. CONCLUSIONS

We describe our photofragment spectrometer, allowing coincidence detection of all possible photodissociation products, including cation, anion, and neutral fragments. From the derived model and simulation of our spectrometer, we observe that anion and cation trajectories exhibit chromatic and spatial aberrations due to the presence of a weak electrostatic lens after the ion-laser interaction region. These aberrations are estimated and corrected by combining an analytic model with the simulated parameters. Using the F_2^- molecular anion as an example, we demonstrated KER reconstruction for four different photofragment processes occurring in the presence of intense laser pulses. Based on the dominant role of the spatial aberrations for asymmetric channels, new data were measured with a lower ion beam width. As predicted by our model, the new data show significant improvement in the KER resolution, allowing us to provide an improved measurement of the F_2^- dissociation energy $D_0 = 1.256 \pm 0.005$ eV.

ACKNOWLEDGMENTS

[1] A. I. Chichinin, K.-H. Gericke, S. Kauczok, and C. Maul, Int. Rev. Phys. Chem. **28**, 607 (2009).
[2] R. E. Continetti, Int. Rev. Phys. Chem. **17**, 227 (1998).
[3] J. Meyer and R. Wester, Annu. Rev. Phys. Chem. **68**, 333 (2017).
[4] *Fragmentation Processes*, edited by C. T. Whelan (Cambridge University Press, Cambridge, 2012).
[5] A. T. J. B. Eppink and D. H. Parker, Rev. Sci. Instrum. **68**, 3477 (1997).
[6] D. Rolles, Z. Pešić, M. Perri, R. Bilodeau, G. Ackerman, B. Rude, A. Kilcoyne, J. Bozek, and N. Berrah, Nucl. Instrum. Methods Phys. Res., Sect. B **261**, 170 (2007).
[7] A. Stolow, A. E. Bragg, and D. M. Neumark, Chem. Rev. **104**, 1719 (2004).
[8] D. Nandi, V. S. Prabhudesai, B. M. Nestmann, and E. Krishnakumar, Phys. Chem. Chem. Phys. **13**, 1542 (2011).
[9] T. Baer, J. Booze, and K.-M. Weitzel, *Vacuum Ultraviolet Photoionization and Photodissociation of Molecules and Clusters* (World Scientific, 1991), pp. 259–296.
[10] A. Lafosse, M. Lebech, J. Brenot, P. Guyon, O. Jagutzki, L. Spielberger, M. Vervloet, J. Houver, and D. Dowek, Phys. Rev. Lett. **84**, 5987 (2000).
[11] R. Dörner, V. Mergel, O. Jagutzki, L. Spielberger, J. Ullrich, R. Moshammer, and H. Schmidt-Böcking, Phys. Rep. **330**, 95 (2000).
[12] J. Ullrich, R. Moshammer, A. Dorn, R. Dorner, L. P. H. Schmidt, and H. Schmidt-Böcking, Rep. Prog. Phys. **66**, 1463 (2003).
[13] T. Jahnke, T. Weber, T. Osipov, A. Landers, O. Jagutzki, L. Schmidt, C. Cocke, M. Prior, H. Schmidt-Böcking, and R. Dörner, J. Electron Spectrosc. Relat. Phenom. **141**, 229 (2004), Frontiers of Coincidence Experiments.
[14] R. S. Gao, P. S. Gibner, J. H. Newman, K. A. Smith, and R. F. Stebbings, Rev. Sci. Instrum. **55**, 1756 (1984).
[15] M. Epshtein, A. Portnov, and I. Bar, Phys. Chem. Chem. Phys. **17**, 19607 (2015).
[16] A. Iqbal, L.-J. Pegg, and V. G. Stavros, J. Phys. Chem. A **112**, 9531 (2008).
[17] K. L. Wells, G. Perriam, and V. G. Stavros, J. Chem. Phys. **130**, 074308 (2009).
[18] D. Strasser, K. Bhushan, H. Pedersen, R. Wester, O. Heber, A. Lafosse, M. Rappaport, N. Altstein, and D. Zajfman, Phys. Rev. A **61**, 60705 (2000).
[19] D. Strasser, L. Lammich, S. Krohn, M. Lange, H. Kreckel, J. Levin, D. Schwalm, Z. Vager, R. Wester, A. Wolf, and D. Zajfman, Phys. Rev. Lett. **86**, 779 (2001).
[20] P. Fechner and H. Helm, Phys. Rev. A **82**, 052523 (2010).
[21] P. C. Fechner and H. Helm, Phys. Chem. Chem. Phys. **16**, 453 (2014).
[22] K. A. Hanold, A. K. Luong, T. G. Clements, and R. E. Continetti, Rev. Sci. Instrum. **70**, 2268 (1999).
[23] R. Otto, J. Ma, A. W. Ray, J. S. Daluz, J. Li, H. Guo, and R. E. Continetti, Science **343**, 396 (2014).
[24] C. J. Johnson, B. B. Shen, B. L. Poad, and R. E. Continetti, Rev. Sci. Instrum. **82**, 105105 (2011).
[25] V. S. Prabhudesai, U. Lev, A. Natan, B. D. Bruner, A. Diner, O. Heber, D. Strasser, D. Schwalm, I. Ben-Itzhak, J. J. Hua, B. D. Esry, Y. Silberberg, and D. Zajfman, Phys. Rev. A **81**, 023401 (2010).
[26] I. Ben-Itzhak, P. Wang, J. Xia, A. Max Sayler, M. A. Smith, J. Maseberg, K. D. Carnes, and B. D. Esry, Nucl. Instrum. Methods Phys. Res., Sect. B **233**, 56 (2005).
[27] U. Lev, V. Prabhudesai, A. Natan, B. Bruner, A. Diner, O. Heber, D. Strasser, D. Schwalm, I. Ben-Itzhak, J. J. Hua, B. D. Esry, Y. Silberberg, and D. Zajfman, J. Phys.: Conf. Ser. **194**, 032060 (2009).
[28] Y. Albeck, D. M. Kandhasamy, and D. Strasser, J. Phys. Chem. A **118**, 388 (2014).
[29] Y. Albeck, D. M. Kandhasamy, and D. Strasser, Phys. Rev. A **90**, 053422 (2014).
[30] Y. Albeck, G. Lerner, D. M. Kandhasamy, V. Chandrasekaran, and D. Strasser, J. Phys. A **120**, 3246 (2016).
[31] Y. Albeck, G. Lerner, D. M. Kandhasamy, V. Chandrasekaran, and D. Strasser, Phys. Rev. A **92**, 061401 (2015).
[32] D. M. Kandhasamy, Y. Albeck, K. Jagtap, and D. Strasser, J. Phys. Chem. A **119**, 8076 (2015).
[33] A. Shahi, Y. Albeck, and D. Strasser, J. Phys. Chem. A **121**, 3037 (2017).
[34] K. Luria, N. Lavie, and U. Even, Rev. Sci. Instrum. **80**, 104102 (2009).
[35] P. W. Harland and J. L. Franklin, J. Chem. Phys. **61**, 1621 (1974).
[36] N. Ruckhaberle, L. Lehmann, S. Matejcik, E. Illenberger, Y. Bouteiller, V. Periquet, L. Museur, C. Desfrançois, and J.-P. Schermann, J. Phys. Chem. A **101**, 9942 (1997).
[37] W. C. Wiley and I. H. McLaren, Rev. Sci. Instrum. **26**, 1150 (1955).
[38] Picoscope 5203, Pico Technology Limited.
[39] Prosilica GE 680, Allied Vision Technologies Canada, Inc.

[40]X. Urbain, D. Bech, J. P. Van Roy, M. Géléoc, S. J. Weber, A. Huetz, and Y. J. Picard, Rev. Sci. Instrum. **86**, 023305 (2015).

[41]S. K. Lee, F. Cudry, Y. F. Lin, S. Lingenfelter, A. H. Winney, L. Fan, and W. Li, Rev. Sci. Instrum. **85**, 123303 (2014).

[42]I. Luzon, K. Jagtap, E. Livshits, O. Lioubashevski, R. Baer, and D. Strasser, Phys. Chem. Chem. Phys. **19**, 13488 (2017).

[43]M. Szilagyi, *Electron and Ion Optics* (Springer Science & Business Media, 2012).

[44]SIMION: Ion optics software, SIS, Inc.

[45]A. Kramida, Y. Ralchenko, J. Reader *et al.*, NIST Atomic Spectra Database, version 5.0, National Institute of Standards and Technology, 2012.